Intersublevel magnetoabsorption in the valence band of *p*-type InAs/GaAs and Ge/Si self-assembled quantum dots

M. Tadić[1,2] and F. M. Peeters[1,*]
[1]*Department of Physics, University of Antwerp, Universiteitsplein 1, B-2610 Antwerpen, Belgium*
[2]*Faculty of Electrical Engineering, University of Belgrade, 11120 Belgrade, Serbia*
(Received 31 July 2004; revised manuscript received 19 November 2004; published 31 March 2005)

The linear intraband (intersublevel) optical magnetoabsorption between the valence-band states in thin disk-shaped self-assembled quantum dots is studied. Strain is modeled with the continuum mechanical approach, while band mixing and the magnetic field are taken into account through the axially symmetric $\mathbf{k}\cdot\mathbf{p}$ model. The absorption spectra in InAs/GaAs and Ge/Si quantum dots are computed for the case when a magnetic field perpendicular to the dot's base is present for both *p*-polarization in the Voigt configuration and *s*-polarization in the Faraday configuration. Due to the selection rules, the transitions between the states which differ by ±1 in the total angular momentum (F_z) dominate for *s*-polarized light, while the transitions between the states of different F_z are strictly forbidden for *p*-polarization. In InAs/GaAs quantum dots, the magnetic field brings about a red shift of the absorption peak for *s*-polarized light, while the absorption peak for *p*-polarization is blue-shifted with respect to the zero field case, and also the absorption curves widen. In Ge/Si, much smaller shifts of the absorption curves due to the magnetic field are found and almost no widening occurs, which is attributed to the larger number of energy levels in Ge/Si dots. The obtained results compare favorably with the spectroscopic measurements at zero magnetic field, especially with regard to the relative energies of the absorption peaks for *s*- and *p*-polarized light.

DOI: 10.1103/PhysRevB.71.125342 PACS number(s): 78.67.Hc, 73.21.La

I. INTRODUCTION

There is a growing interest in quantum dots, which are expected to have numerous possible applications, like lasers and photonic detectors.[1,2] The zero-dimensional density of states in quantum dots allows for absorption of arbitrary polarized light, which has a great advantage over quantum wells, where absorption of in-plane polarized light in the conduction band is prohibited. In the valence band of the quantum well, however, band mixing lifts this shortcoming, but the larger effective mass of holes decreases the photoresponse of *p*-type doped quantum-well infrared photodetectors (QWIP's). In order to take full advantage of the low conduction electron effective mass, quantum dot infrared photodetectors (QDIP's) are usually doped with donors, and usually rely on discrete-to-continuum transitions.[2,3] Discrete-to-discrete intersubband transitions occur in intersubband spectroscopy, which has emerged as a powerful tool to probe the electronic structure of quantum wells and dots.[4–6] To explain spectroscopic data, discrete-to-discrete intersublevel absorption should be appropriately modeled which is the aim of the present paper. For example, in *p*-type doped quantum dots, band mixing should be taken into account, and also the strain distribution, if the structure is grown on a lattice mismatched substrate. The discrete-to-discrete intersubband transitions in the valence band of quantum wells were treated in Ref. 7 for the first time. Subsequently, the discrete-to-continuum intersubband transitions in the valence band of quantum wells, aiming to explain the photocurrent measurements on *p*-type doped QWIP's were considered.[8,9] It has been recently demonstrated that by coping with the valence band intersubband transitions one may rely on band mixing to tailor the optical properties of a nanostructure.[10]

Quantum dots are most efficiently formed by the Stranski-Krastanow mode of epitaxial growth. Due to strain fields, these structures self-assemble in vertical stacks. Quantum dots of various shapes and sizes, and also of various materials, have been fabricated by this method, but InAs quantum dots grown on a GaAs substrate have been most comprehensively studied to date. Because of the unperfect control of the dot's size, intersublevel absorption lines in the conduction band of an InAs/GaAs self-assembled quantum dot (SAQD) are subject to strong inhomogeneous broadening.[5,6] Another interesting system to realize QDIP's is *p*-type doped Ge/Si.[11,12] Intersubband transitions in the valence band of Ge/Si quantum wells are promising for lasing in the THz range.[13] For a similar case of three dimensional confinement, there has been a quest to realize so-called quantum-dot cascade lasers.[14–16] For the much more explored quantum-well cascade lasers, it has been shown that the external magnetic field is beneficial for their performance.[17–21] The theoretical study of the influence of a magnetic field on quantum-dot cascade lasers has been tackled only very recently.[14] Treatments of SAQD's in presence of a magnetic field, including strain and band mixing, are practically nonexistent. A notable exception is Ref. 22, where the magnetoluminescence spectra were modeled. Recently, intersublevel transitions in *n*-type doped InAs/GaAs SAQD's, including both mixing and strain but in the absence of an external magnetic fields were addressed theoretically.[23]

In this paper, a model for discrete-to-discrete intersublevel absorption in the valence band of cylindrical SAQD's is presented. In contrast to previous works, we consider intersublevel transitions between the holes, and also include an ex-

ternal magnetic field directed perpendicularly to the dot's base. The continuum mechanical approach is adopted to model the strain distribution, which is then entered into the multiband $\mathbf{k}\cdot\mathbf{p}$ theory of the valence-band electronic structure. The variations of the transition matrix elements with the magnetic field are determined. Selection rules are ascertained for both the Faraday configuration, where in-plane (s) polarized light is incident on the sample, and the Voigt configuration, where we assume p-polarization. The influence of the magnetic field on the absorption-line shape is examined. The results are compared with the previously published experimental results on linear absorption in p-type doped SAQD's of similar geometry as analyzed here.[5,6]

The paper is organized as follows. In Sec. II, the models of strain and electronic structure are briefly explained. The model for intersublevel absorption is discussed in Sec. III. The results of our calculation are given and discussed in Sec. IV. Our conclusions are given in Sec. V. In the appendix we give the matrix elements and selection rules needed in the calculation of the intersublevel absorption.

II. STRAIN AND THE SINGLE-PARTICLE ELECTRONIC STRUCTURE

The strain distribution is extracted from the three-dimensional continuum mechanical model, in which the displacements are discretized by means of first-order finite elements onto a nonuniform mesh. The model is explained in detail in Refs. 24 and 25. For a small average number of holes in the quantum dot, like 1-2, the intersublevel absorption may be computed in the single hole picture, without losing details at the scale of 100 meV of the photon energy. The 6×6 multiband Pikus-Bir Hamiltonian H, which consists of the kinetic part H_k, the strain part H_s, and the potential V due to the band offset at the dot-barrier interface, i.e.,

$$H = H_k + H_s + V, \tag{1}$$

is used to compute the vb states. H_k and H_s have the same form,[26,27]

$$H_{k,s} = \begin{bmatrix} E_{hh+} & \sqrt{2}S & -S & 0 & -R & -\sqrt{2}R \\ \sqrt{2}S^{\dagger} & E_{lh+} & \sqrt{2}Q_{-} & R & 0 & \sqrt{3}S \\ -S^{\dagger} & \sqrt{2}Q_{-} & E_{so+} & \sqrt{2}R & -\sqrt{3}S & 0 \\ 0 & R^{\dagger} & \sqrt{2}R^{\dagger} & E_{hh-} & \sqrt{2}S^{\dagger} & -S^{\dagger} \\ -R^{\dagger} & 0 & -\sqrt{3}S^{\dagger} & \sqrt{2}S & E_{lh-} & \sqrt{2}Q_{+} \\ -\sqrt{2}R^{\dagger} & \sqrt{3}S^{\dagger} & 0 & -S & \sqrt{2}Q_{+} & E_{so-} \end{bmatrix}, \tag{2}$$

with the matrix elements additionally labeled by k and s, respectively. Both H_k and H_s are modified to establish the full axial symmetry of the Hamiltonian, which in V is enforced by an assumed cylindrical shape of the dot.[24] The matrix elements of H_k are given by

$$E_{hh\pm k} = P_k + Q_k \mp 3\kappa\mu_B B, \tag{3a}$$

$$E_{lh\pm k} = P_k - Q_k \mp \kappa\mu_B B, \tag{3b}$$

$$E_{so\pm k} = P_k - \Delta \mp (1+2\kappa)\mu_B B, \tag{3c}$$

$$P_k = -\frac{\hbar^2}{2m_0}\gamma_1(k_x^2 + k_y^2 + k_z^2), \tag{3d}$$

$$Q_{\pm k} = Q_k \pm M_z \tag{3e}$$

$$Q_k = -\frac{\hbar^2}{2m_0}\gamma_2(k_x^2 + k_y^2 - 2k_z^2), \tag{3f}$$

$$M_z = (1+\kappa)\mu_B B, \tag{3g}$$

$$R_k = \frac{\hbar^2}{2m_0}\sqrt{3}\frac{\gamma_2+\gamma_3}{2}k_-^2, \tag{3h}$$

$$S_k = \frac{\hbar^2}{2m_0}\sqrt{6}\gamma_3 k_- k_z, \tag{3i}$$

where k_x, k_y, and k_z denote the components of the vb electron wave vector along the [100], [010], and [001] crystallographic direction, respectively, $k_\pm = k_x \pm ik_y$, γ_1, γ_2, γ_3, and κ are the Luttinger parameters, Δ is the spin-orbit split-off energy, μ_B is the Bohr magneton, and B is the magnetic field, oriented along the z direction.

In H_s, the shear strains and the difference between ε_{xx} and ε_{yy} in the off-diagonal terms are neglected, and moreover all diagonal strain tensor components are averaged over the polar angle in cylindrical coordinates. Such modifications deliver axially symmetric H_s, which contains the following matrix elements:

$$E_{hh+s} = E_{hh-s} = P_s + Q_s, \tag{4a}$$

$$E_{lh+s} = E_{lh-s} = P_s - Q_s, \tag{4b}$$

$$E_{sos} = P_s, \tag{4c}$$

$$P_s = a_v(\overline{\varepsilon_{xx}} + \overline{\varepsilon_{yy}} + \overline{\varepsilon_{zz}}), \tag{4d}$$

$$Q_{+s} = Q_{-s} = \frac{b}{2}(\overline{\varepsilon_{xx}} + \overline{\varepsilon_{yy}} - 2\overline{\varepsilon_{zz}}), \tag{4e}$$

$$R_s = 0, \tag{4f}$$

$$S_s = 0. \tag{4g}$$

Here, a_v and b denote the deformation potentials for the valence band, while $\overline{\varepsilon_{xx}}$, $\overline{\varepsilon_{yy}}$, and $\overline{\varepsilon_{zz}}$ are angular averages of the diagonal strain tensor components. The effect of the piezoelectric field on the electronic structure of flat quantum dots is small,[2] therefore it is neglected in the present model. Moreover, the thin wetting layer is disregarded in the model, since it affects mainly the states near the energy continuum.

The magnetic field is taken into account in the symmetric gauge. In Eq. (2), it is convenient to introduce k_+ and k_-,

$$k_{\pm} = k_x \pm ik_y = -i\,\exp(\pm i\varphi)\left(\frac{\partial}{\partial\rho} \pm \frac{i}{\rho}\frac{\partial}{\partial\varphi} \mp \frac{\rho}{2l_c^2}\right), \quad (5)$$

instead of k_x and k_y. In Eq. (5), φ and ρ are the polar angle and the radial coordinate, respectively, while $l_c=\sqrt{\hbar/(eB)}$ denotes the magnetic length (e is the elementary charge).

The envelope functions are expanded into a basis which consists of products of 10 ρ-dependent Bessel functions and 100 sin/cos functions along the z direction. Furthermore, the symmetry with respect to the $z=0$ plane is used to alleviate the computation of eigenstates. The z component of the total angular momentum $F_z=f_z\hbar$ and the state's parity, denoted here as $\mathcal{P}$, are good quantum numbers for a vb electron. To each envelope function, there corresponds the envelope angular momentum $L=l_\nu\hbar$ ($\nu=1, 2, \ldots, 6$) for a given F_z. For the state with the eigenenergy E_i, the νth envelope function has the form:

$$F_{i\nu}(\varphi,\rho,z) = \frac{1}{\sqrt{2\pi}}\Psi(\rho,z)e^{il_{i\nu}\varphi}. \quad (6)$$

The envelope function spinor for the even vb state has the form

$$\begin{bmatrix} F_{i1} \\ F_{i2} \\ F_{i3} \\ F_{i4} \\ F_{i5} \\ F_{i6} \end{bmatrix} = \begin{bmatrix} \Psi_{i1}^{+}e^{il_{i1}\varphi} \\ \Psi_{i2}^{-}e^{il_{i2}\varphi} \\ \Psi_{i3}^{-}e^{il_{i3}\varphi} \\ \Psi_{i4}^{-}e^{il_{i4}\varphi} \\ \Psi_{i5}^{+}e^{il_{i5}\varphi} \\ \Psi_{i6}^{+}e^{il_{i6}\varphi} \end{bmatrix} = \begin{bmatrix} \Psi_{i1}^{+}e^{i(f_z-3/2)\varphi} \\ \Psi_{i2}^{-}e^{i(f_z-1/2)\varphi} \\ \Psi_{i3}^{-}e^{i(f_z-1/2)\varphi} \\ \Psi_{i4}^{-}e^{i(f_z+3/2)\varphi} \\ \Psi_{i5}^{+}e^{i(f_z+1/2)\varphi} \\ \Psi_{i6}^{+}e^{i(f_z+1/2)\varphi} \end{bmatrix}, \quad (7)$$

where the parities are explicitly labeled in the superscripts, and are reversed for the odd state. Note that the zone-center basis functions are arranged as in Ref. 24. In addition to f_z and $\mathcal{P}$, the lowest $|l_\nu|=X$ among six bands is used in the symbol $X_{f_z}^{\mathcal{P}}$ to denote the vb state.

III. TRANSITION MATRIX ELEMENTS AND INTERSUBLEVEL ABSORPTION

The appropriate quantity to describe the intersublevel absorption in quantum dots is the effective cross section[28]

$$\sigma(\hbar\omega) = \frac{\pi}{n\epsilon_0 c\omega A}\sum_{i,f}|\langle F_f|H_{\rm int}|F_i\rangle|^2 \times \Xi(E_i,E_f,\hbar\omega)[f_{\rm FD}^{(h)}(E_i) - f_{\rm FD}^{(h)}(E_f)], \quad (8)$$

where n denotes the index of refraction, ϵ_0 is the vacuum permittivity, c is the speed of light, $\hbar\omega$ is the photon energy, A is the intensity of the magnetic vector potential of the light wave, indices i and f are for the initial and the final state, respectively, F_i and F_f denote the valence band envelope function spinors of the two states, while E_i and E_f denote their energies. $H_{\rm int}$ is the interaction Hamiltonian elaborated below, and $f_{\rm FD}^{(h)}$ is the Fermi-Dirac distribution function for the holes. The Fermi level is obtained as the solution of the equation

$$N_h = \sum_{\mathcal{P},f_z,m} f_{\rm FD}^{(h)}(E_{\mathcal{P},f_z,m}), \quad (9)$$

for a given number of holes per quantum dot N_h.

In the absence of broadening, like due to interaction with polar optical phonons, Ξ takes the form $\delta(E_i-E_f-\hbar\omega)$. The interaction with optical phonons, as an example, leads to homogeneous broadening, described by the Lorentzian of width Γ,

$$\Xi(E_i,E_f,\hbar\omega) = \frac{\Gamma/(2\pi)}{(E_f-E_i-\hbar\omega)^2+\Gamma^2/4}. \quad (10)$$

The existence of a phonon bottleneck, due to the zero dimensional density of states, was predicted some time ago.[29] However, it was argued that the model of weak coupling between electrons and phonons in quantum dots is dubious, and was subsequently replaced by a model based on polarons.[30–32] The intersublevel relaxation time in the valence band of a single InAs/GaAs SAQD was measured recently.[33] More recently, it was determined that the polaron decay depends on the transition energy, which is accounted for by the finite lifetime of the phonon in a polaron.[2,32] Description of the real process of electron-photon interaction in the phonon bath is beyond the scope of the devised model, and therefore a simple relaxation-time approximation is adopted to describe the line broadening. However, the shape of the absorption line in fabricated quantum-dot ensembles is dominantly affected by the spread of the dot size,[5,6] which brings about inhomogeneous broadening due to energy levels variation. In order to model such system, we employ the Gaussian distribution function

$$\Xi(E_i,E_f,\hbar\omega) = \frac{1}{\sqrt{2\pi}\Gamma}\exp\left(-\frac{(E_f-E_i-\hbar\omega)^2}{2\Gamma^2}\right). \quad (11)$$

The interaction Hamiltonian is given by

$$H_{\rm int} = eA\mathbf{e}\cdot\mathbf{v}, \quad (12)$$

where $\mathbf{v}=\nabla_{\mathbf{k}}H/\hbar$ denotes the velocity operator and $\mathbf{e}$ is the unit polarization vector of light. Note that the interaction Hamiltonian is derived in the Coulomb gauge, which is a special case of the symmetric gauge employed for the electronic structure calculation. In the following, we consider the matrix element $M=\langle F_f|\mathbf{e}\nabla_{\mathbf{k}}H|F_i\rangle$. For s-polarized light, there exists an in-plane anisotropy of the intersublevel absorption, which is not relevant for our axially symmetric model of the electronic structure, and therefore we decided to average the modulus squared of the matrix element over the polar angle θ of $\mathbf{e}$ in the cylindrical coordinates. The calculation of the transition matrix element for s-polarized light $|M_\perp|^2$ proceeds along the lines listed below:

(1) The kernel of the transition matrix element $\mu_\perp$ ($M_\perp=\int_\Omega\mu_\perp d\Omega$) is written as

$$\mu_\perp = \sum_{k=1}^{4} F_f^\dagger O_{\perp k}F_i\Theta_{\perp k}(\theta,\varphi) + \sum_{k=1}^{2} F_f^\dagger\Pi_{\perp k}F_i\Phi_{\perp k}(\varphi). \quad (13)$$

$O_{\perp k}$ and $\Pi_{\perp k}$ denote the *overlap and dipole matrices* (with respect to the z direction), given in Tables VII and VIII of

Appendix B, respectively. The in-plane anisotropy of the transition matrix element is contained in $\Theta_{\perp k}$, shown in Table VII, hence it affects only the overlap part of the matrix element. The dipole matrix elements are selected by $\Phi_{\perp k}$ functions, shown in Table VIII.

(2) $\partial/\partial\varphi$ is replaced by its eigenvalue $il_{i\nu}$, and the integrals over ϕ in the transition matrix elements are evaluated analytically. The $l_{i\nu}$ is extracted for a given f_z of the initial state and the index ν is arranged by overlap or dipole matrix. The integrals over ρ and z are computed numerically. It turns out that the transition matrix elements are given as linear combinations of the *component matrix elements*, which are classified as overlap integrals,

$$o = \int_0^{R_t} \rho d\rho \int_{-H_z}^{+H_z} dz \Psi_{fm'} \hat{O} \Psi_{im}, \tag{14}$$

and dipole matrix elements,

$$\pi = \int_0^{R_t} \rho d\rho \int_{-H_z}^{+H_z} dz \Psi_{fm'} \zeta \Psi_{im}. \tag{15}$$

In Eqs. (14) and (15), $\hat{O}$ denotes either ξ or υ, defined in Eqs. (B1) and (B2), respectively, the operator ζ is given in Eq. (B3), R_t and $2H_z$ denote the radius and the height of the cylinder employed to expand the envelope functions of the vb states in quantum dots, and m and m' are number of the states which take part in the overlap integrals and dipole matrix elements. The component matrix elements are additionally labeled by subscripts $\perp$ for s-polarized light and $\parallel$ for p-polarized light. For the later use, we denote the numbers of the nonzero matrix elements in $O_{\perp k}$ and $\Pi_{\perp k}$ by $n_{\perp Ok}$ and $n_{\perp\Pi k}$, respectively.

(3) $|M_\perp|^2$ is formed as linear combination of $o^*_{\perp kj} o_{\perp k'j'}$, $\pi^*_{\perp kj} o_{\perp k'j'}$, and $\pi^*_{\perp kj} \pi_{\perp k'j'}$ terms, where j counts the nonzero matrix elements in $O_{\perp k}$ and $\Pi_{\perp k}$. The coefficients which multiply these terms depend not only on θ but also on the orbital momenta of the two envelope functions which participate in the component matrix elements.

(4) The coefficients in $|M_\perp|^2$ are averaged over θ, which gives selection rules for the envelope angular momenta of the envelope functions used to compute the products $o^*_{\perp kj} o_{\perp k'j'}$ and $\pi^*_{\perp kj} o_{\perp k'j'}$. These rules are expressed by matrices Δ and Λ, given in Eqs. (C1) and (C2), respectively.

The expression for the in-plane average of the matrix element $\overline{|M_\perp|^2}$ derived according to the previous procedure reads ($D_{kk'} = \Delta_{kk'}(1) + \Delta_{kk'}(-1)$)

$$\begin{aligned}\overline{|M_\perp|^2} = {} & \frac{1}{4}\sum_{k=1}^{4}\sum_{j=1}^{n_{\perp ok}} |o_{\perp kj}|^2 (\delta_{l'_j, l_j - 1} + \delta_{l'_j, l_j + 1}) + \sum_{k=1}^{2} |\pi_{\perp kj}|^2 \delta_{l'_j, l_j} \\ & + 2\sum_{k=1}^{4}\sum_{j=1}^{n_{\perp Ok}}\sum_{j'>j}^{n_{\perp Ok}} \mathrm{Re}(o^*_{\perp kj} o_{\perp kj'} D_{kk}) \\ & + 2\sum_{k=1}^{4}\sum_{k'=1}^{k}\sum_{j=1}^{n_{\perp Ok}}\sum_{j'=1}^{n_{\perp Ok'}} \mathrm{Re}(o^*_{\perp kj} o_{\perp k'j'} D_{kk'}) \\ & + 2\sum_{k'=1}^{2}\sum_{k=1}^{4}\sum_{j=1}^{n_{\perp\Pi k}}\sum_{j'=1}^{n_{\perp O'_k}} \mathrm{Re}(\pi^*_{\perp k'j'} o_{\perp kj} \Lambda_{kk'}) \\ & + 2\sum_{k=1}^{2}\sum_{j=1}^{n_{\perp\Pi k}}\sum_{j'>j}^{n_{\perp\Pi k}} \mathrm{Re}(\pi^*_{\perp kj} \pi_{\perp kj'}) \delta_{l'_{j'}, l_{j'}} \delta_{l'_j, l_j}. \end{aligned} \tag{16}$$

For p-polarized light, there is no dependence on θ, therefore the matrix element $M_\parallel$, is much easier to calculate. Its kernel is given by

$$\mu_\parallel = \sum_{k=1}^{2} F_f^\dagger O_{\parallel k} F_i \Theta_{\parallel k}(\varphi) + F_f^\dagger \Pi_\parallel F_i. \tag{17}$$

The overlap matrices $O_{\parallel k}$ and functions $\Theta_{\parallel k}$ are given in Table IX of Appendix B. Here, it is not necessary to expand the modulus squared of the matrix element, and also the selection rules are much simpler. Hence,

$$M_\parallel = \sum_{j=1}^{n_{\parallel O1}} o_{\parallel 1j} \delta_{l'_j, l_j - 1} + \sum_{j=1}^{n_{\parallel O2}} o_{\parallel 2j} \delta_{l'_j, l_j + 1} + \sum_{j=1}^{n_{\parallel\Pi}} \pi_{\parallel j} \delta_{l'_j, l_j}, \tag{18}$$

with the symbols having similar meanings as in Eq. (16). It is easy to prove that irrespective of the values of f_z of the initial and the final state, the equal parity states produce zero $M_\parallel$. Therefore, the expression for $M_\parallel$ is simplified to

$$M_\parallel = \sum_{j=1}^{n_{\parallel\Pi}} \pi_{\parallel j} \delta_{l'_j, l_j}, \tag{19}$$

where $n_{\parallel\Pi} = 10$, as Eqs. (B8) and (B11) indicate. Because of the structure of $\Pi_\parallel$ and the selection rule for the envelope angular momenta, only the states of equal f_z produce finite $M_\parallel$.

IV. RESULTS AND DISCUSSION

The model is applied to InAs/GaAs and Ge/Si quantum dots with base radius $R = 8$ nm and height $h = 3$ nm. Such p-doped InAs/GaAs and Ge/Si SAQD's were fabricated recently.[5,6,12] The material parameters for the two dots are given in Table I. The average number of holes per quantum dot amounts to 2 in our calculation. For the Lorentzian, Eq. (10), we use $\Gamma = 1.88$ meV, which corresponds to the recently measured intraband relaxation time $\tau = 0.7$ ps in InAs/GaAs SAQD's,[33] and the same value is adopted for the Ge/Si SAQD. For the Gaussian curve, Eq. (11), $\Gamma = 20$ meV seems to be a reasonable choice. The magnetic field spans the range $0 \leqslant B \leqslant 40$ T, while all states of sizable contribution to absorption in the range $-9/2 \leqslant f_z \leqslant 9/2$ are taken into account when computing the intersublevel absorption. For the temperature we choose $T = 77$ K. The envelope functions are expanded onto a cylinder of radius $R_t = 32$ nm and height $2H_z = 80$ nm. No compositional mixing between the dot and the barrier material is taken into account. Zero energy is taken to be at the top of the valence band in the matrix, and the energy axis points upwards from the valence to the conduction band.

TABLE I. Material parameters of GaAs, InAs, Si, and Ge, relevant for the calculation of intersublevel absorption in the valence band of InAs/GaAs and Ge/Si SAQD's. All the values for GaAs and InAs are taken from Ref. 34, and for Si and Ge from Ref. 35 except where it is explicitly indicated.

Parameter	GaAs	InAs	Si	Ge
Δ (eV)	0.341	0.39	0.044	0.297
γ_1	6.98	20.00	4.285	13.38
γ_2	2.06	8.5	0.339	4.24
γ_3	2.93	9.2	1.446	5.69
κ	1.28[g]	7.68[h]	−0.26[h]	3.41[h]
a_c (eV)	−7.17	−5.08	−5.10	−9.50
a_v (eV)	1.16	1.00	0	0
b (eV)	−2.0	−1.8	−2.1	−2.9
d (eV)	−4.8	−3.6	−4.85	−5.28
n	3.255[a,i]	3.51[i]	3.38[b,i]	4[i]
a (nm)	0.565325[c]	0.60583[d]	0.54304[e]	0.56598[f]
C_{11} (10^{10} N/m^2)	12.21	8.329	16.75	13.15
C_{12} (10^{10} N/m^2)	6.498	0.494	5.66	4.526
C_{44} (10^{10} N/m^2)	8.007	0.684	6.00	3.959

[a] $T=0$ K value; $n(T)=3.255(1+4.5\times10^{-5}T)$.
[b] $T=0$ value; $n(T)=3.38(1+3.9\times10^{-5}T)$.
[c] $T=300$ K value; $a(T)=0.565325+3.88\times10^{-6}(T-300\text{ K})$.
[d] $T=300$ K value; $a(T)=0.60583+2.74\times10^{-6}(T-300\text{ K})$.
[e] $T=298.15$ K value; $a(T)=0.54304+1.8138\times10^{-5}(T-298.15\text{ K})+1.542\times10^{-9}(T-298.15\text{ K})^2$.
[f] $T=300$ K value; $a(T)=0.56598+4.14\times10^{-6}(T-300\text{ K})$.
[g] Reference 36
[h] Reference 37.
[i] Reference 35.

A. Hole states and transition matrix elements

If the magnitude of any l_ν in the νb envelope function spinor is zero, the ground state of the holes may be obtained. Such situation arises in the $S^{\pm}_{\pm3/2}$ and $S^{\pm}_{\pm1/2}$ states, where the orbital momentum of the heavy hole (hh) and light hole equals (lh) zero, respectively. Furthermore, most bright absorption lines are due to transitions which involve states of these two symmetries, therefore their energy levels in InAs/GaAs SAQD are shown in Figs. 1(a) and 1(b), and for Ge/Si SAQD in Figs. 2(a) and 2(b). In the absence of the magnetic field, $X^{\pm}_{\pm f_z}$ states are degenerate with $X^{\mp}_{\mp f_z}$ states, but $B>0$ lifts the degeneracy. Fermi level, shown by the dotted-dashed curves in Figs. 1 and 2, is computed for the two holes in the quantum dot. Because of the compressive strain and the larger effective mass of the heavy holes, $1S^{+}_{+3/2}$ and $1S^{-}_{-3/2}$ states have the highest energies in both quantum dots in the whole explored range of B, and the lowest energy states of the other angular momenta are well separated in InAs/GaAs SAQD. In practice, only these two states are populated for the chosen acceptor density in InAs/GaAs.

In contrast, for Ge/Si SAQD the $1S^{+}_{+1/2}$ and $1S^{-}_{-1/2}$ states shown in Fig. 2(b) are not far from the pair of ground states displayed in Fig. 2(a), and therefore some population of the $f_z=\pm1/2$ states may be expected at 77 K, the temperature which we considered in our calculation. The increase of the $1S^{-}_{-3/2}$ energy above the $1S^{+}_{+3/2}$ level does not seem to be unusual if one recalls that the envelope function F_4 (for the heavy holes) in the $1S^{-}_{-3/2}$ state is even. $1S^{+}_{+3/2}$ and $1S^{-}_{-3/2}$ states split by a rather small amount in InAs/GaAs SAQD, and even smaller (virtually zero) splitting is found in Ge/Si quantum dots. In the $S^{\pm}_{\pm1/2}$ states, zero envelope orbital momentum belongs to the light holes, which have lower energies due to strain, and also a larger splitting with respect to the $S^{\pm}_{\pm3/2}$ states. The νb states in all shells do not exhibit anticrossings, except for the states near the energy continuum.

The overlap matrices for s-polarized light, shown in Table VII of Appendix B, and Δ_{oo} functions, given in Eq. (C1), favor transitions between equal-parity states with ±1 difference in f_z, as shown in Table II. The three largest $\overline{|M_\perp|^2}$ at zero-field, and also the three largest $\overline{|M_\perp|^2}$ for the transitions from the $1S^{+}_{+3/2}$ state, are displayed in Table II, with the rank of the $1S^{+}_{+3/2}$-derived transitions displayed in the boxes. The envelope angular momenta in all displayed states guarantee a nonzero value for $\overline{|M_\perp|^2}$, which may be large for the transitions which include not only the $S^{\pm}_{\pm3/2}$ and $S^{\pm}_{\pm1/2}$ but also $P^{\pm}_{\pm5/2}$ and $D^{\pm}_{\pm7/2}$ states. The transitions which do not satisfy $f_z=f'_z\pm1$ and have opposite parity are also allowed by the dipole matrices in Eq. (13), but rather low $\overline{|M_\perp|^2}$ is computed for them. When deriving Eq. (19), we explained that only the states of equal f_z and opposite parity give $|M_\parallel|^2\neq0$, as shown in Table III for the InAs/GaAs SAQD, where the largest matrix elements are displayed, and also where the transitions from $1S^{\pm}_{\pm3/2}$ states are explicitly labeled in boxes. Slightly different order of the largest transition matrix elements in the

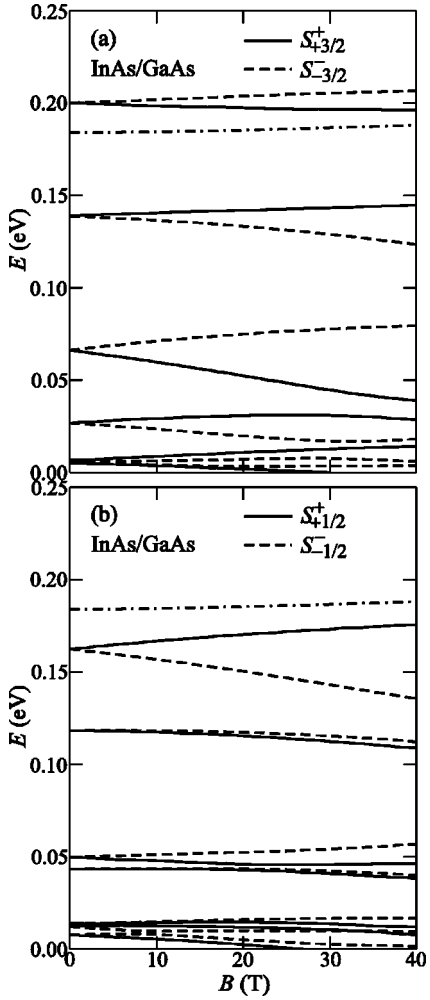

FIG. 1. The energy spectrum in the valence band of InAs/GaAs single quantum dot as it varies with the magnetic field: (a) $S^{\pm}_{\pm 3/2}$ and (b) $S^{\pm}_{\pm 1/2}$ states. Even and odd hole states are shown by the solid and dashed lines, while the dotted-dashed lines denote the position of the Fermi level. The energy is measured from the valence-band top in the matrix upwards.

TABLE II. Three largest optical transition matrix elements in InAs/GaAs quantum dots for *s*-polarized light. Each transition is accompanied with its Kramers counterpart, which occurs between states of reversed total angular momentum and opposite parity. Rank of the hole transition from the $1S^+_{+3/2}$ states, which are shown in Fig. 4, is displayed in boxes.

Rank	Transition	E_{if} (meV)	$\overline{\lvert M_\perp \rvert^2}$ (10^{-3} eV^2 nm^2)
1	$1S^+_{+1/2}-3S^+_{-1/2}$	111.59	9.85
2	$1P^+_{+5/2}-4S^+_{+3/2}$	136.23	8.46
3,[1]	$1S^+_{+3/2}-1P^+_{+5/2}$	37.10	5.18
[2]	$1S^+_{+3/2}-6S^+_{+1/2}$	188.13	5.02
[3]	$1S^+_{+3/2}-7S^+_{+1/2}$	192.50	3.23

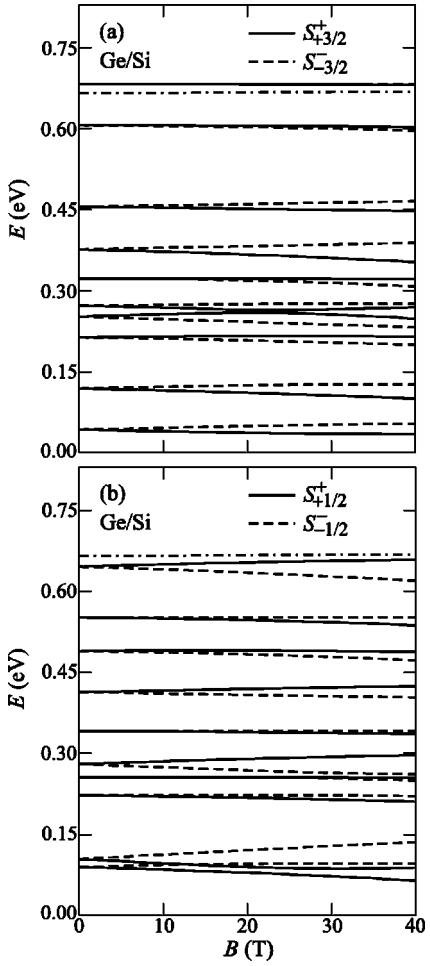

FIG. 2. The same as in Fig. 1, but for Ge/Si quantum dots: (a) $S^{\pm}_{\pm 3/2}$ and (b) $S^{\pm}_{\pm 1/2}$ states.

Ge/Si quantum dot is found, as Tables IV and V show for *s*- and *p*-polarized light, respectively.

In order to illustrate the localization of the hole wave functions, the effective potentials for the *hh*, *lh*, and the split-off (*so*) band along the *x* direction are plotted in Fig. 3(a) for InAs/GaAs SAQD. Because of the strain and the band offset, the heavy holes are confined within the dot, while the light holes are expelled towards the lateral surface of the dot. The confinement of the *so* holes is established by means of mixing with the *lh* band. The $1S^{\pm}_{\pm 3/2}$ states are only populated for the assumed two holes in the InAs/GaAs SAQD, and therefore we show their probability density in Fig. 3(b), where the *hh*, *lh*, and *so* components are resolved, and the percentage of contribution of each band in the total probability density of the holes is explicitly given in the figure. The *hh* hole cloud, whose peak is located in the center of the dot, gives the dominant contribution to the probability density, while the *lh* and *so* hole clouds are substantially smaller. The probability density of the $1P^+_{+5/2}$ hole state, which makes the largest matrix element for *s*-polarized light, is plotted in Fig. 3(c). Here, a larger *lh* contribution is found than in the initial $1S^+_{+3/2}$ state. As inferred from Eqs. (B4) and (B5) and the composition of the states shown in Fig. 3, only a few component overlap integrals are relevant for the transition matrix

TABLE III. The same as in Table II, but for *p*-polarized light.

Rank	Transition	E_{if} (meV)	$\lvert M_{\parallel}\rvert^2$ (10^{-3} eV^2 nm^2)
1, 1	$1S^{+}_{+3/2}-4S^{-}_{+3/2}$	148.90	4.95
2	$1P^{+}_{+5/2}-4P^{-}_{+5/2}$	148.18	4.18
3	$1S^{+}_{+1/2}-3S^{-}_{+1/2}$	111.59	3.30
2	$1S^{+}_{+3/2}-5S^{-}_{+3/2}$	190.05	2.79
3	$1S^{+}_{+3/2}-2S^{-}_{+3/2}$	128.19	1.72

element for *s*-polarized light. These are the overlaps between (1) the *hh* envelope functions, (2) between the *hh* and *lh* envelope functions, and (3) between the *lh* envelope functions. Comparison of Figs. 3(b) and 3(c) reveals that the overlap between the *hh* envelope functions of the $1P^{+}_{+5/2}$ state and the *lh* envelope functions of the $1S^{+}_{+3/2}$ state produces the main part in the transition matrix element, while the overlaps between the two *lh* envelope functions give a much smaller contribution, and only tails of the *hh* hole clouds overlap in this matrix element. In contrast, for *p*-polarization, the main part of the dipole matrix element is due to the *hh* envelope functions of the states which take part in the transition. As already shown, the $1S^{+}_{+3/2}-4S^{-}_{+3/2}$ transition and its Kramers degenerate counterpart produce the largest transition matrix elements, and therefore the probability density in the $4S^{-}_{+3/2}$ state is displayed in Fig. 3(d). Like for the $1S^{+}_{+3/2}$ state, the F_1 function dominate in the $4S^{-}_{+3/2}$ state, hence the dipole matrix element between them offers the largest transition matrix element for *p*-polarized light, as indicated by the dipole matrix given by Eq. (B11).

In addition to the hole energy levels, the matrix elements squared take different values with increasing magnetic field, as illustrated in Fig. 4(a) for the three largest $\overline{\lvert M_{\perp}\rvert^2}$ where the initial hole state has $S^{\pm}_{\pm 3/2}$ symmetry in the InAs/GaAs quantum dot. The population of only the $1S^{+}_{+3/2}$ and $1S^{-}_{-3/2}$ states demonstrated in Fig. 1 reduces the contribution of the other transition matrix elements. The transition energies $E_{if}=E_f-E_i$, shown in Fig. 4(b), are also affected by the magnetic field. The energy shifts are less than about 20 meV for fields up to 40 T. In each pair, one $\overline{\lvert M_{\perp}\rvert^2}$ increases with *B*, and can reach a maximum, while the value of the other counterpart decreases, taking extremely low values for some transitions. The latter effect is the result of the spatial separation of the hole envelope functions of the states involved in the transitions. The effects of the magnetic field on $\lvert M_{\parallel}\rvert^2$ and associated E_{if}, shown in Figs. 4(c) and 4(d), are similar to the case for *s*-polarization, and similar values of the matrix element squared are obtained. The values of the largest transition matrix elements displayed in Fig. 4 are similar for *s*- and *p*-polarized light, but the transition energies differ. For *s*-polarized light, energies of the transition 1 is close to 40 meV, while the transitions marked 2 and 3 are close to 200 meV, which is near the energy continuum. Here we note that discrete-to-continuum transitions in quantum wells by rule result in a lower absorption coefficient than the discrete-to-discrete transitions. For the large transition matrix element in quantum dots, however, not only the spatial localization of the envelope functions need to be appropriate, but also the hole orbital momenta should be favorable. In other words, the transition matrix elements to the highly localized states in the dot may be reduced by the selection rules. Other states positioned near the energy continuum, where considerable spill-over of the envelope function in the matrix occurs, are then the only ones which contribute to the absorption.

TABLE IV. The same as in Table II, but for Ge/Si SAQD.

Rank	Transition	E_{if} (meV)	$\overline{\lvert M_{\perp}\rvert^2}$ (10^{-3} eV^2 nm^2)
1	$1P^{+}_{+5/2}-3S^{+}_{+3/2}$	186.45	21.85
2, 1	$1S^{+}_{+3/2}-3S^{+}_{+1/2}$	193.40	18.25
3	$1S^{+}_{+1/2}-3S^{+}_{-1/2}$	181.33	17.91
2	$1S^{+}_{+3/2}-1P^{+}_{+5/2}$	40.74	5.60
3	$1S^{+}_{+3/2}-11S^{+}_{+1/2}$	625.74	3.79

The three largest (at $B=0$) values of $\overline{\lvert M_{\perp}\rvert^2}$ for the total angular momentum of the initial state $3\hbar/2$ in Ge/Si SAQD's, shown in Fig. 5(a), vary like those in the InAs/GaAs SAQD's, although they are substantially larger, and the transition energies shown in Fig. 5(a) split by similar amount [compare Figs. 5(b) and 4(b)]. However, the transition energies are higher and $\overline{\lvert M_{\perp}\rvert^2}$ is larger here, which may be ascribed to the better confinement in Ge/Si SAQD's. Figures 5(c) and 5(d) show $\lvert M_{\parallel}\rvert^2$ and E_{if} in the Ge/Si SAQD for *p*-polarized light.

B. Intersublevel absorption spectrum

The absorption spectrum is affected by the demonstrated variation of the transition matrix elements and the energies in the external magnetic field. The homogeneously broadened absorption lines in the InAs/GaAs quantum dots for *s*-polarized light in the low-energy ($0<\hbar\omega<120$ meV) and high-energy (120 meV$<\hbar\omega<200$ meV) ranges are shown in Figs. 6(a) and 6(b), respectively, while the absorption for *p*-polarized light and homogeneous broadening is shown in Fig. 6(c), respectively. A few highest absorption lines are explicitly labeled in the figures. The relatively long relaxation time and zero-dimensional character of the holes bring about narrow absorption lines. For *s*-polarized light, the dominant peak at $E_{if}=37.35$ meV is due to the $1S^{+}_{+3/2}-1P^{+}_{+5/2}$ and $1S^{-}_{-3/2}-1P^{-}_{-5/2}$ transitions, ranked 1 in Table II, which is almost merged with the $1S^{+}_{+3/2}-1S^{+}_{+1/2}$ and $1S^{-}_{-3/2}-1S^{-}_{-1/2}$ pair of transitions. In the range between 120 and 200 meV, there exist a few absorption peaks with an order of magnitude lower absorption than the peaks positioned below 40 meV. The absorption near 200 meV corresponds to transitions to levels which are near the top of the valence band in the matrix, where the result may be modified by the presence of the wetting layer, which was not included in our theoretical model. The largest contribution for 120 meV$<E_{if}<200$ meV is found from the $1S^{+}_{+3/2}-6S^{+}_{+1/2}$ (ranked 2 in Table II), $1S^{+}_{+3/2}-3S^{+}_{+1/2}$, and $1S^{+}_{+3/2}-7S^{+}_{+1/2}$ (ranked 3 in

TABLE V. The same as in Table II, but for Ge/Si SAQD and *p*-polarized light.

Rank	Transition	E_{if} (meV)	$\lvert M_{\parallel}\rvert^2$ (10^{-3} eV^2 nm^2)
1	$3D^{+}_{-7/2}-8D^{-}_{-7/2}$	332.99	51.56
2	$1S^{+}_{-1/2}-7S^{-}_{-1/2}$	358.72	48.60
3	$1S^{+}_{-3/2}-8S^{-}_{-3/2}$	371.29	41.62
[1]	$1S^{+}_{+3/2}-4S^{-}_{+3/2}$	300.85	38.03
[2]	$1S^{+}_{+3/2}-8S^{-}_{+3/2}$	462.85	9.11
[3]	$1S^{+}_{+3/2}-9S^{-}_{+3/2}$	591.28	5.64

Table II) transitions and their Kramers counterparts. The fourth and fifth bright absorption line arise due to the $1S^{+}_{+3/2}-4S^{+}_{+1/2}$ and $1S^{+}_{+3/2}-4P^{+}_{+5/2}$ transitions, which are located at $E_{if}=157$ meV and $E_{if}=182$ meV. For *p*-polarized light, the brightest line is due to the transitions $1S^{-}_{-3/2}-4S^{+}_{-3/2}$ and $1S^{+}_{+3/2}-4S^{-}_{-3/2}$ ($\lvert M_{\parallel}\rvert^2$ marked [1] in Table III). A lower effective cross section is computed at 190 meV, where the transitions $1S^{+}_{+3/2}-5S^{-}_{+3/2}$ and $1S^{-}_{-3/2}-5S^{+}_{-3/2}$, whose $\lvert M_{\parallel}\rvert^2$ is second ([2]) in magnitude in Table III, take place. The third absorption peak is found at 128 meV and it arises from the transitions $1S^{+}_{+3/2}-2S^{-}_{+3/2}$ and $1S^{-}_{-3/2}-2S^{+}_{-3/2}$ (marked [3] in Table III).

Since the magnetic field reduces the matrix element of one of the Kramers degenerate transitions, the other starts to contribute to the absorption, as shown by the dashed line in the left part of Fig. 6(a). Furthermore, the absorption lines in the energy range $\hbar\omega<40$ meV are redshifted with respect to their positions at $B=0$. In fact, the $1S^{-}_{-3/2}-1P^{-}_{-5/2}$ transition produces the highest absorption line, positioned at 32.1 meV, while the second peak is found from the $1S^{+}_{+3/2}-1S^{+}_{+1/2}$ transition, and it is positioned at 20.4 meV, which is already in the far-infrared region of the electromagnetic spectrum. Thus, the magnetic field may shift the absorption lines in QDIP to energies below the optical phonon resonance in bulk ($\sim$36 meV). This energy range is interesting for the THz detectors, which was recently discussed for the case of quantum wells.[38] For *p*-polarized light, depicted by the dashed line in Fig. 6(c), the magnetic field of 40 T slightly redshifts the dominant absorption lines. Because of the reduced absorption on its Kramers counterpart, we found that the absorption line at 160 meV in Fig. 6(c) originates only from the $1S^{-}_{-3/2}-3S^{+}_{-3/2}$ transition, but $\lvert M_{\parallel}\rvert^2$ is enlarged considerably [see Fig. 4(c)], therefore σ in this peak is larger than at $B=0$. Another peak, positioned at $\hbar\omega=192$ meV for $B=40$ T, arises from both the $1S^{+}_{+3/2}-5S^{-}_{+3/2}$ and $1S^{-}_{-3/2}-5S^{+}_{-3/2}$ transitions (labeled [2] in Table III), which are very close to each other, and does not shift tremendously when the magnetic field increases, as Fig. 4(d) shows.

If the inhomogeneous broadening is taken into account, the low energy absorption lines overlap to dominate in the energy spectrum for *s*-polarized light, therefore σ increases

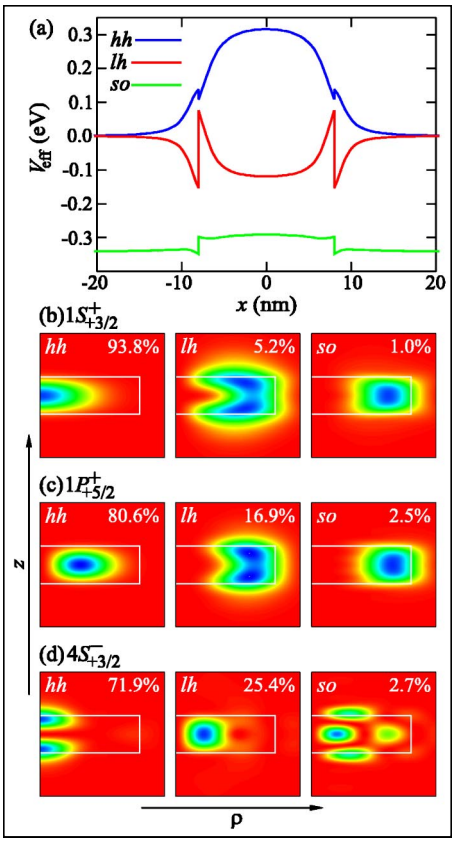

FIG. 3. (Color online) (a) The effective potentials for the *hh* (blue line), the *lh* (red line), and the *so* band (green line) in InAs/GaAs SAQD, where the dot radius is $R=8$ nm, and the height is $h=3$ nm. The probability densities of (a) the $1S^{+}_{+3/2}$ state, (b) the $1P^{+}_{5/2}$ state, and (c) the $4S^{-}_{+3/2}$ state. The states displayed in (b) and (c) have the largest transition matrix elements for the initial $1S^{+}_{+3/2}$ state at $B=0$ in the case of *s*- and *p*-polarized light. The dot boundary is indicated by the solid white line.

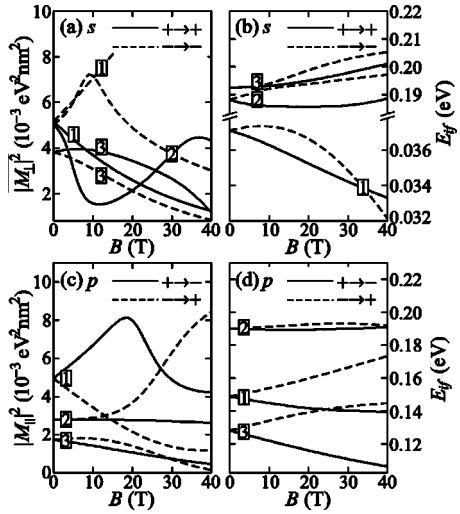

FIG. 4. The dominant transition matrix elements (left panel) and the transition energies (right panel) in the valence band of InAs/GaAs single quantum dot as they vary with the magnetic field. Parity of the states is symbolically denoted by + and − sign, while the full state's symmetry is shown in Tables II and III. The three transitions for *s*-polarization (upper panel), (a) $\lvert M_{\perp}\rvert^2$, (b) E_{if}. The three transitions for *p*-polarization (lower panel), (c) $\lvert M_{\parallel}\rvert^2$, (b) E_{if}.

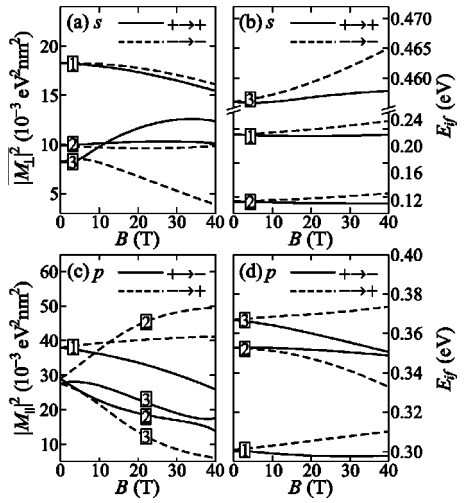

FIG. 5. The same as Fig. 4, but for the three dominant transitions in Ge/Si quantum dots. The symmetry of the states is shown in Tables IV and V. *s*-polarization (upper panel), (a) $\overline{|M_\perp|^2}$, (b) the transition energies E_{if}. *p*-polarization (lower panel), (c) $|M_\parallel|^2$, (d) E_{if}.

considerably as $\hbar\omega$ decreases below 40 meV, while no large transition matrix elements with $E_{if}<40$ meV, allow σ to decay as $\hbar\omega$ tends to zero. For the two polarizations, the absorption spectra do not differ much at $B=0$, and σ has similar values in the peaks, which are separated by a rather small amount of photon energy. These absorption peaks are located at 179 and 142 meV for *s*- and *p*-polarized light, respectively. The enlargement of some transition matrix elements by the magnetic field, makes the absorption spectrum wider, while the height of the absorption peaks lower only slightly. At $B=40$ T, the absorption peak for *s*-polarized light is redshifted by 19 meV, while the absorption peak for *p*-polarized light is blueshifted by 5 meV. These changes might be inferred from Figs. 6(a) and 6(b).

The different features in the homogeneously broadened absorption spectra of Ge/Si SAQD's are of similar origin as those found in InAs/GaAs SAQD's. This is also shown by the explicit labels of the transition lines in Figs. 7(a)–7(c). Furthermore, σ for $\hbar\omega<40$ meV and $B=0$ exhibit peaks of comparable magnitude to those in InAs/GaAs SAQD's, although much larger $\overline{|M_\perp|^2}$ and $|M_\parallel|^2$ were found in Ge/Si SAQD's. This is a consequence of the absence of strong transition matrix elements which include the $1S^{\pm}_{\pm 3/2}$ state in this energy range. The dominant peak for *s*-polarized light at 40.8 meV, shown in Fig. 7(a), arises from the $1S^{+}_{+3/2}-1P^{+}_{+5/2}$ and $1S^{-}_{-3/2}-1P^{-}_{-5/2}$ transitions. It is separated by a few meV from the absorption line due to the $1S^{+}_{+3/2}-1S^{+}_{+1/2}$ and $1S^{-}_{-1/2}-1S^{-}_{-1/2}$ transitions. We previously found that these four transitions merge in InAs/GaAs SAQD's to form the brightest absorption line below 40 meV. On the high energy side in Fig. 7(a) ($\sim$200 meV), the absorption peak is positioned at 192 meV and arises from the $1S^{+}_{+3/2}-3S^{+}_{+1/2}$ and $1S^{-}_{-3/2}-3S^{-}_{-3/2}$ transitions. For still higher energies, there exist absorption lines with much lower oscillator strength. In the low energy range ($\hbar\omega<350$ meV), shown in Fig. 7(b), *p*-polarized light is dominantly absorbed by means of the $1S^{+}_{+3/2}-4S^{-}_{+3/2}$ and $1S^{-}_{-3/2}-4S^{+}_{-3/2}$ transitions, which was also found for InAs/GaAs SAQD's, but here the peak of σ is located at 300 meV as shown in Fig. 7. At photon energies $\hbar\omega>350$ meV, there are several resonances, displayed in Fig. 7(c), which are mostly due to the transitions between the populated $1S^{\pm}_{\pm 3/2}$ and empty $1S^{\mp}_{\mp 3/2}$ states with high principal quantum number. But, as enabled by the close Fermi level to the initial $1S^{+}_{+1/2}$ state [see Fig. 2(b)], the $1S^{+}_{+1/2}-7S^{-}_{+1/2}$ transition matrix element, located at $E_{if}=385$ meV gives a non-negligible absorption line. When compared with the InAs/GaAs SAQD's, all absorption lines are shifted to higher energies, which we attribute to the larger *vb* offset in the Ge/Si SAQD's.

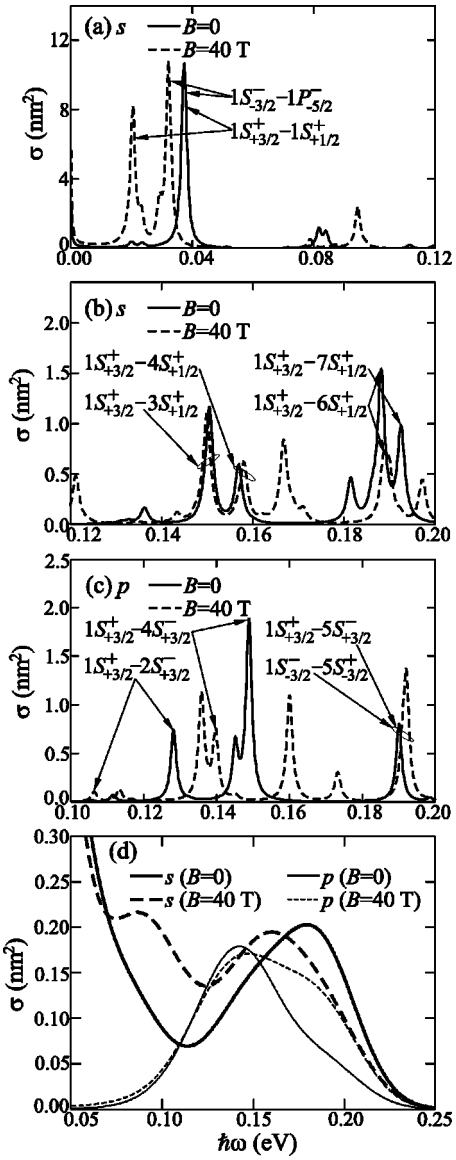

FIG. 6. The intersublevel absorption spectra in InAs/GaAs self-assembled quantum dots at $B=0$ (solid lines) and $B=40$ T (dashed lines). *s*-polarization and homogeneous broadening for (a) 0 meV $<\hbar\omega<$ 120 meV and (b) 120 meV $<\hbar\omega<$ 200 meV. (c) *p*-polarization and homogeneous broadening. (d) The case of inhomogeneous broadening. The highest absorption lines are explicitly labeled.

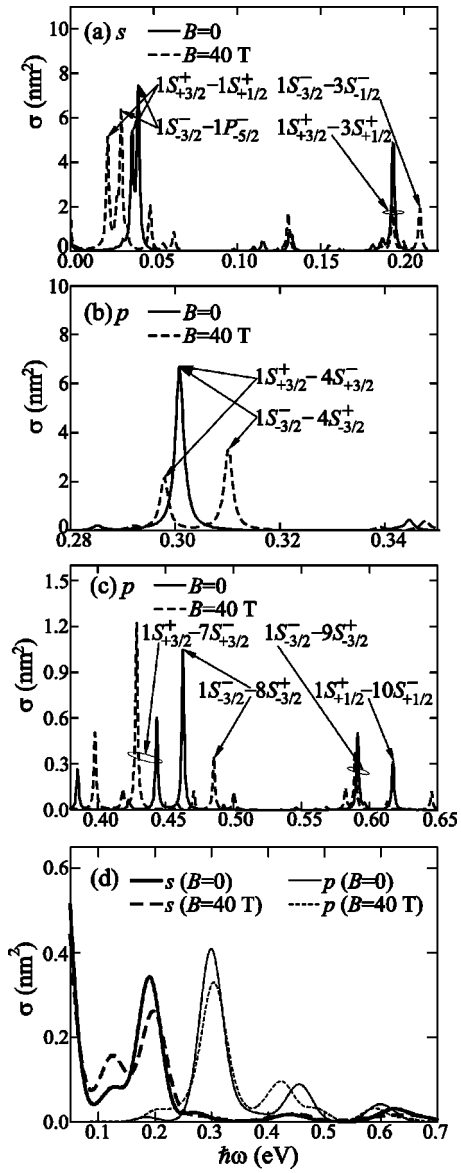

FIG. 7. The same as in Fig. 6, but now for a Ge/Si single quantum dot. The case of inhomogeneous broadening for (a) *s*-polarization, (b) *p*-polarization in the energy range 280 meV $<\hbar\omega<$ 350 meV, and (c) *p*-polarization in the energy range 380 meV $<\hbar\omega<$ 650 meV. (d) The absorption for inhomogeneous broadening and for both *s*- and *p*-polarized light.

For nonzero magnetic field, the positions of the absorption lines below 40 meV, shown by the dashed curve in Fig. 7(a), decrease. On the high energy side ($\sim$200 meV), the main contribution to the absorption line positioned at 193 meV arises from the $1S^{+}_{+3/2}-3S^{+}_{+3/2}$ and $1S^{-}_{-3/2}-3S^{-}_{-3/2}$ transitions. The magnetic field splits the dominant absorption line for *p*-polarized light at $\hbar\omega=300$ meV, shown in Fig. 7(b), into two lines, separated by 12 meV. At the high-energy side of the photon energy, the absorption of *p*-polarized light, shown in Fig. 7(c), exhibit a few changes related to the changes of the transition energies between the relevant states, but no large increase of the absorption and only small energy shifts of the absorption lines are observed.

The inhomogeneous broadening smears out the large changes observed in the absorption spectra in Figs. 7(a)–7(c). As shown in Fig. 7(d), the low-energy transitions increase the absorption of *s*-polarized light as $\hbar\omega$ tends to zero, while no similar variation is found for *p*-polarized light. Furthermore, as the result of a large band offset, several absorption peaks in the near-infrared region are found for both polarizations. Splitting of the transition energies in the magnetic field and their increase, slightly blueshifts the main absorption peaks. Furthermore, the absorption peak near 126 meV [see the thick dashed line in Fig. 7(d)] rises by means of the magnetic field, which is attributed to the redshift of the low-energy transition energies by the finite magnetic field.

Let us briefly compare qualitatively the results of our calculation with the measurements performed on lens-shaped InAs/GaAs quantum dots, which have slightly different size, but similar volume as adopted here (around 600 nm^3). The absorption peaks for *s*- and *p*-polarized light at 165 and around 110 meV, respectively, were measured using intersubband spectroscopy,[5,6] while for the same polarizations 179 and 142 meV are computed in our model for zero magnetic field. We find that the mutual position of the two peaks are well reproduced in our model. The discrepancy between theory and experiment arises due to the different geometry and shapes of SAQD's which were used. For *s*-polarized light, the single band model used in Ref. 6 demonstrated the existence of transitions at 133 and 188 meV, but failed to reproduce the *s*-polarized transition at 165 meV, which was tentatively ascribed to the position of the absorption peak in Ref. 6. In our multiband $\mathbf{k}\cdot\mathbf{p}$ calculation, we observe more than two absorption lines, namely at 150, 157, 182, and 188 meV. Therefore, our model indicates that the position of the inhomogeneously broadened absorption peak does not coincide with any bright line, but is a result of the overlap of a few of them. We conclude that our model (without using any fitting parameter) produces important refinements to the simple single-band model, and offers plausible results which compare favorably with experiment. At this moment, to the best of our knowledge, no experimental results on the magnetic field dependence of the hole intersublevel transitions in SAQD's, are available, and consequently our theoretical results may be considered as predictions.

V. CONCLUSION

The intersublevel absorption spectrum in *p*-type cylindrical InAs/GaAs and Ge/Si self-assembled quantum dots in the presence of an external magnetic field perpendicular to the dot's base was calculated. The strain and the large effective mass of heavy holes favors the population of $f_z=\pm 3/2$ states by holes, therefore they chiefly contribute to the absorption. The homogeneously broadened sharp absorption lines for *s*- and *p*-polarized light are found in the midinfrared spectral range. When inhomogeneous broadening is active, the low-energy transition matrix elements between the highest-energy *vb* states which differ by ± 1 in f_z increase the absorption of the *s*-polarized light in the far-infrared range. The absence of similar peaks for *p*-polarized light leads to a

decay of the spectrum for the effective cross section when the photon energy decreases. Such difference in the response for *s*- and *p*-polarized light is a consequence of the small height and the large radius of the quantum dots, for which the ground states of different f_z (favorable for the absorption of *s*-polarized light) are close to each other. The magnetic field removes Kramers degeneracy between transition matrix elements and their energies, and mostly increases one counterpart of the Kramers pair and decreases the other. In the InAs/GaAs SAQD, the redshift of the low-energy transitions and the increase of their matrix elements causes a redshift of the inhomogeneously broadened absorption spectrum for *s*-polarized light. On the contrary, transition energies for *p*-polarized light are blueshifted by the magnetic field and a few of them have comparably large magnitudes, which leads to the blueshift and widening of the inhomogeneously broadened absorption line. In Ge/Si SAQD, a few distinct peaks located in the near-infrared region of the electromagnetic spectrum are found.

Our theory explains the experimental absorption spectra as to be a result of the overlap of several optical transitions. Furthermore, the transition energies found in our calculation agree well with previously published single-band calculations,[6] but our $\mathbf{k}\cdot\mathbf{p}$-based model disclose more details in the absorption spectra of *p*-type doped SAQD's. Even though, the fabricated SAQD's have different geometry and size (but the same volume), a favorable comparison with experiment was established. Moreover, by reducing the spread of the dot's size during the growth, we showed that the absorption may be shifted towards the THz spectral range. The advantage of *p*-type quantum dots is the existence of a large number of energy levels, which may be shifted by the magnetic field to enhance the absorption in certain ranges of photon energies.

ACKNOWLEDGMENTS

This work was supported in part by the European Commission GROWTH program NANOMAT project, Contract No. G5RD-CT-2001-00545, the Serbian Ministry of Science, the University of Antwerp (GOA and VIS), the Belgian Science Policy, and the EU-NoI: SANDiE. M.T. would like to thank Professor John Davies for useful discussions.

APPENDIX A: MATRIX ELEMENTS OF THE HAMILTONIAN MATRIX

We expand the Ψ functions given in Eq. (6) in products of the ρ-dependent functions

$$g_{n(l)}(\rho) = \frac{\sqrt{2}}{R_t}\frac{1}{|J_{|l|+1}(k_{n(l)}R_t)|}J_l(k_{n(l)}\rho). \tag{A1}$$

and functions which depend on *z*,

$$f_m^+(z) = \frac{1}{\sqrt{H_z}}\cos\left(\frac{m\pi}{2H_z}z\right), \quad m = 1,3,5,\ldots, \tag{A2a}$$

$$f_m^-(z) = \frac{1}{\sqrt{H_z}}\sin\left(\frac{m\pi}{2H_z}z\right), \quad m = 2,4,6\ldots. \tag{A2b}$$

TABLE VI. Matrix elements between *g* and *f* functions used in the calculation of the Hamiltonian matrix.

Type	Expression
$\mu_{\rho,1}$	$\langle g_{n'(l')}\|\frac{\partial}{\partial\rho}\|g_{n(l)}\rangle$
$\mu_{\rho,2}$	$\langle g_{n'(l')}\|\frac{1}{\rho}\|g_{n(l)}\rangle$
$\mu_{\rho,3}$	$\langle g_{n'(l')}\|\rho\|g_{n(l)}\rangle$
$\mu_{\rho,4}$	$\langle g_{n'(l')}\|\frac{\partial^2}{\partial\rho^2}\|g_{n(l)}\rangle$
$\mu_{\rho,5}$	$\langle g_{n'(l')}\|\frac{1}{\rho}\frac{\partial}{\partial\rho}\|g_{n(l)}\rangle$
$\mu_{\rho,6}$	$\langle g_{n'(l')}\|\frac{1}{\rho^2}\|g_{n(l)}\rangle$
$\mu_{\rho,7}$	$\langle g_{n'(l')}\|g_{n(l)}\rangle$
$\mu_{\rho,8}$	$\langle g_{n'(l')}\|\rho^2\|g_{n(l)}\rangle$
$\mu_{\rho,9}$	$\langle g_{n'(l')}\|\rho\frac{\partial}{\partial\rho}\|g_{n(l)}\rangle$
$\mu_{z,0}$	$\langle f_{m'}\|f_m\rangle$
$\mu_{z,1}$	$\langle f_{m'}\|\frac{d}{dz}\|f_m\rangle$
$\mu_{z,2}$	$\langle f_{m'}\|\frac{d^2}{dz^2}\|f_m\rangle$

The parts of the Hamiltonian matrix elements which originate from H_s and V are computed numerically, while H_k allows some analytical work. Each linear combination in H_k, denoted hereafter by η, is constant within the dot and also in the matrix, but has a steplike variation at the boundary. Consequently, matrix elements of H_k consist of boundary terms originating from the derivatives of η and those where η is a scaling function. The expression for the latter reads

$$M_{\eta,i,j} = \eta_m\mu_{\rho m,i}\mu_{zm,j} + (\eta_d - \eta_m)\mu_{\rho d,i}\mu_{zd,j}. \tag{A3}$$

The subscripts in the one-dimensional matrix elements μ refer to the coordinate (ρ or *z*), the domain of integration (*m* and *d*), and the type of the matrix element, listed in Table VI.

The parts of the Hamiltonian matrix elements, which arise from the variation of η at the dot-matrix interface, depend on one of the following functions:

$$\Delta_{\rho,0} = -Rg_{n'(l')}(R)g_{n(l)}(R), \tag{A4a}$$

$$\Delta_{\rho,1} = -Rg_{n'(l')}(R)\left.\frac{dg_{n(l)}}{d\rho}\right|_{\rho=R}, \tag{A4b}$$

$$\Delta_{z,0} = f_{m'}(-d)f_m(-d) - f_{m'}(+d)f_m(+d), \tag{A4c}$$

$$\Delta_{z,1} = f_{m'}(-d)\left.\frac{df_m}{dz}\right|_{-d} - f_{m'}(d)\left.\frac{df_m}{dz}\right|_{+d}. \tag{A4d}$$

1. Matrix elements due to E_{hh}, E_{lh}, E_{so}, and Q_k [Eqs. (3a)–(3d) and (3f)]

All diagonal matrix elements of the multiband Hamiltonian and Q_k may be written as

$$D_k = \eta_\rho(k_x^2 + k_y^2) + \eta_z k_z^2, \tag{A5}$$

where η_ρ and η_z are the multiplying coefficients. It is straightforward to prove

$$k_x^2 + k_y^2 = k_+ k_- + \frac{1}{l_c^2}. \tag{A6}$$

By using Eq. (5), the ρ dependent part of the operator D takes the form

$$D_\rho = \eta_\rho(k_x^2 + k_y^2) \rightarrow -\eta_\rho\frac{\partial^2}{\partial\rho^2} - \frac{\eta_\rho}{\rho}\frac{\partial}{\partial\rho} - \frac{\eta_\rho}{\rho^2}\frac{\partial^2}{\partial\varphi^2} - \frac{\partial\eta_\rho}{\partial\rho}\frac{\partial}{\partial\rho} + \eta_\rho\frac{\rho^2}{4l_c^4} - -i\frac{\eta_\rho}{l_c^2}\frac{\partial}{\partial\rho}. \tag{A7}$$

The matrix element of D_ρ is given by

$$M_{D_\rho} = \langle l'n'm'|D_\rho|lnm\rangle = \delta_{l-l'}\left(-M_{\eta_\rho,4,0} - M_{\eta_\rho,5,0} + l^2 M_{\eta_\rho,5,0} + \frac{1}{l_c^2}M_{\eta_\rho,7,0} + \frac{1}{4l_c^4}M_{\eta_\rho,8,0} - (\eta_{\rho d} - \eta_{\rho m})\Delta_{\rho,1}\mu_{zd,0}\right), \tag{A8}$$

where l and l' denotes the order of the Bessel functions, n and n' are indices of the zeros of Bessel functions, and m and m' are the indices of sin/cos expansion functions for the z direction.

The z dependent part of D_k,

$$D_z = \eta_z k_z^2 \rightarrow -\frac{\partial\eta_z}{\partial z}\frac{\partial}{\partial z} - \eta_z\frac{\partial^2}{\partial z^2}, \tag{A9}$$

produces the matrix element

$$M_{D_z} = \langle l'n'm'|D_z|lnm\rangle = \delta_{l-l'}[-M_{\eta_z,7,2} - (\eta_{zd} - \eta_{zm})\Delta_{z,1}\mu_{\rho d,7}]. \tag{A10}$$

2. Matrix elements due to S_k [Eq. (3i)]

In order to compute S_k defined in Eq. (3i), we use Eq. (5), and employ symmetrization, to obtain

$$S_k = \frac{\hbar^2}{2m_0}\frac{\sqrt{6}}{2}e^{-i\varphi}\left(-\frac{\rho}{2l_c^2}\frac{\partial\gamma_3}{\partial z} - \frac{\partial\gamma_3}{\partial z}\frac{\partial}{\partial\rho} + \frac{i}{\rho}\frac{\partial}{\partial\varphi}\frac{\partial\gamma_3}{\partial z} - 2\gamma_3\frac{\rho}{2l_c^2}\frac{\partial}{\partial z} - \frac{\partial\gamma_3}{\partial\rho}\frac{\partial}{\partial z} + \frac{2i}{\rho}\gamma_3\frac{\partial^2}{\partial\varphi\,\partial z} - 2\gamma_3\frac{\partial^2}{\partial\rho\,\partial z}\right). \tag{A11}$$

The matrix element is given by

$$\langle l'n'm'|S_k|lnm\rangle = \frac{\hbar^2}{2m_0}\frac{\sqrt{6}}{2}\delta_{l-1-l'}\sum_{i=1}^{7}M_{Si}, \tag{A12}$$

where

$$M_{S1} = -\frac{1}{2l_c^2}(\gamma_{3d} - \gamma_{3m})\Delta_{z,0}\mu_{\rho d,3}, \tag{A13a}$$

$$M_{S2} = -(\gamma_{3d} - \gamma_{3m})\Delta_{z,0}\mu_{\rho d,1}, \tag{A13b}$$

$$M_{S3} = -l(\gamma_{3d} - \gamma_{3m})\Delta_{z,0}\mu_{\rho d,2}, \tag{A13c}$$

$$M_{S4} = -\frac{1}{l_c^2}M_{\gamma_3,3,1}, \tag{A13d}$$

$$M_{S5} = -(\gamma_{3d} - \gamma_{3m})\Delta_{\rho,0}\mu_{zd,1}, \tag{A13e}$$

$$M_{S6} = -2lM_{\gamma_3,2,1}, \tag{A13f}$$

$$M_{S7} = -2M_{\gamma_3,1,1}. \tag{A13g}$$

3. Matrix elements due to R_k [Eq. (3h)]

The R_k matrix element in Eq. (2) in cylindrical coordinates is given by

$$R_k = \frac{\hbar^2}{2m_0}\sqrt{3}e^{-i2\varphi}\left(-\frac{\rho^2}{4l_c^4}\overline{\gamma} - \frac{\rho}{2l_c^2}\frac{\partial\overline{\gamma}}{\partial\rho} + \frac{1}{\rho}\overline{\gamma}\frac{\partial}{\partial\rho} - \frac{\rho}{l_c^2}\overline{\gamma}\frac{\partial}{\partial\rho} - \frac{\partial\overline{\gamma}}{\partial\rho}\frac{\partial}{\partial\rho} - \overline{\gamma}\frac{2i}{\rho^2}\frac{\partial}{\partial\varphi} + \frac{i}{l_c^2}\overline{\gamma}\frac{\partial}{\partial\varphi} + \frac{i}{\rho}\frac{\partial\overline{\gamma}}{\partial\rho}\frac{\partial}{\partial\varphi} - \overline{\gamma}\frac{\partial^2}{\partial\rho^2} + \frac{\overline{\gamma}}{\rho^2}\frac{\partial^2}{\partial\varphi^2} + \frac{2i}{\rho}\overline{\gamma}\frac{\partial^2}{\partial\varphi\,\partial\rho}\right), \tag{A14}$$

where $\overline{\gamma}=(\gamma_2+\gamma_3)/2$. Matrix elements due to the R_k operator in the multiband Hamiltonian are composed of the nine terms,

$$\langle l'n'm'|R_k|lnm\rangle = \frac{\hbar^2}{2m_0}\sqrt{3}\delta_{l-2-l'}\sum_{i=1}^{9}M_{Ri}, \tag{A15}$$

which are given by

$$M_{R1} = -\frac{1}{4l_c^4}M_{\overline{\gamma},8,0}, \tag{A16a}$$

TABLE VII. The four overlap matrices for s-polarized light.

k	$O_{\perp k}$	$\Theta_{\perp k}$
1	$\begin{bmatrix} G_{\perp O} & 0 \\ 0 & G_{\perp O}\end{bmatrix}\xi$	$\sin(\theta-\varphi)$
2	$\begin{bmatrix} 0 & C_{\perp O} \\ -C_{\perp O} & 0\end{bmatrix}\gamma_2\xi - \begin{bmatrix} 0 & C_{\perp O} \\ C_{\perp O} & 0\end{bmatrix}\gamma_3\upsilon$	$\sin(\theta+\varphi)$
3	$\begin{bmatrix} G_{\perp O} & 0 \\ 0 & G_{\perp O}\end{bmatrix}i\upsilon$	$\cos(\theta-\varphi)$
4	$\begin{bmatrix} 0 & C_{\perp O} \\ C_{\perp O} & 0\end{bmatrix}i\gamma_3\xi + \begin{bmatrix} 0 & -C_{\perp O} \\ C_{\perp O} & 0\end{bmatrix}i\gamma_2\upsilon$	$\cos(\theta+\varphi)$

TABLE VIII. The dipole matrices for *s*-polarized light.

k	$\Pi_{\perp k}$	$\Phi_{\perp k}$
1	$\begin{bmatrix} D_{\perp\Pi} & K_{\perp\Pi} \\ 0 & D^T_{\perp\Pi} \end{bmatrix}\gamma_3\zeta$	$\exp(-i\varphi)$
2	$\begin{bmatrix} D^T_{\perp\Pi} & 0 \\ -K_{\perp\Pi} & D_{\perp\Pi} \end{bmatrix}\gamma_3\zeta$	$\exp(+i\varphi)$

$$M_{R2} = -\frac{1}{2l_c^2}(\overline{\gamma}_d - \overline{\gamma}_m)R\Delta_{\rho,0}\mu_{zd,0}, \tag{A16b}$$

$$M_{R3} = (1-2l)M_{\overline{\gamma},5,0}, \tag{A16c}$$

$$M_{R4} = -\frac{1}{l_c^2}M_{\overline{\gamma},9,0}, \tag{A16d}$$

$$M_{R5} = -(\overline{\gamma}_d - \overline{\gamma}_m)\Delta_{\rho,1}\mu_{zd,0}, \tag{A16e}$$

$$M_{R6} = l(2-l)M_{\overline{\gamma},6,0}, \tag{A16f}$$

$$M_{R7} = -\frac{l}{l_c^2}M_{\overline{\gamma},7,0}, \tag{A16g}$$

$$M_{R8} = -(\overline{\gamma}_d - \overline{\gamma}_m)\frac{l}{R}\Delta_{\rho,0}\mu_{zd,0}, \tag{A16h}$$

$$M_{R9} = -M_{\overline{\gamma},4,0}. \tag{A16i}$$

APPENDIX B: OVERLAP AND DIPOLE MATRICES

All overlap and dipole matrices depend only on three operators $|M_\perp|^2$ and $|M_z|^2$,

$$\xi = \frac{\hbar^2}{2m_0}\left(2\frac{i}{\rho}\frac{\partial}{\partial\varphi} - \frac{\rho}{l_c^2}\right), \tag{B1}$$

$$\upsilon = \frac{\hbar^2}{m_0}\frac{\partial}{\partial\rho}, \tag{B2}$$

and

$$\zeta = \frac{\hbar^2}{2m_0}k_z. \tag{B3}$$

Furthermore, the overlap and diagonal matrices are separated into the 3×3 block-matrices.

1. *s*-polarization

For *s*-polarization we define

$$G_{\perp O} = \begin{bmatrix} (\gamma_1+\gamma_2) & 0 & 0 \\ 0 & (\gamma_1-\gamma_2) & \sqrt{2}\gamma_2 \\ 0 & \sqrt{2}\gamma_2 & \gamma_1 \end{bmatrix}, \tag{B4}$$

TABLE IX. The overlap matrices for *p*-polarized light.

k	$O_{\parallel k}$	$\Theta_{\parallel k}$
1	$\begin{bmatrix} D_{\parallel O} & K_{\parallel O} \\ 0 & D^T_{\parallel O} \end{bmatrix} i\gamma_3(-\xi+\upsilon)$	$\exp(-i\varphi)$
2	$\begin{bmatrix} D^T_{\parallel O} & 0 \\ -K_{\parallel O} & D_{\parallel O} \end{bmatrix} i\gamma_3(\xi+\upsilon)$	$\exp(+i\varphi)$

$$C_{\perp O} = \begin{bmatrix} 0 & -\sqrt{3} & -\sqrt{6} \\ \sqrt{3} & 0 & 0 \\ \sqrt{6} & 0 & 0 \end{bmatrix}, \tag{B5}$$

$$D_{\perp\Pi} = \begin{bmatrix} 0 & 2\sqrt{3} & -\sqrt{6} \\ 0 & 0 & 0 \\ 0 & 0 & 0 \end{bmatrix}, \tag{B6}$$

and

$$K_{\perp\Pi} = \begin{bmatrix} 0 & 0 & 0 \\ 0 & 0 & 3\sqrt{2} \\ 0 & -3\sqrt{2} & 0 \end{bmatrix}. \tag{B7}$$

The overlap matrices and dipole matrices are shown in Tables VII and VIII, respectively.

2. *p*-polarization

For *p*-polarized light, we define

$$G_{\parallel\Pi} = \begin{bmatrix} -(\gamma_1-2\gamma_2) & 0 & 0 \\ 0 & -(\gamma_2+2\gamma_2) & 2\sqrt{2}\gamma_2 \\ 0 & 2\sqrt{2}\gamma_2 & -\gamma_1 \end{bmatrix}, \tag{B8}$$

$$D_{\parallel O} = \begin{bmatrix} 0 & -\sqrt{3} & \sqrt{3/2} \\ 0 & 0 & 0 \\ 0 & 0 & 0 \end{bmatrix}, \tag{B9}$$

and

$$K_{\parallel O} = \begin{bmatrix} 0 & 0 & 0 \\ 0 & 0 & -3/\sqrt{2} \\ 0 & 3/\sqrt{2} & 0 \end{bmatrix}. \tag{B10}$$

The overlap matrices for *p*-polarized light are given in Table IX. The dipole matrix for *p*-polarized light is given by

$$\Pi_\parallel = 2\begin{bmatrix} G_{\parallel\Pi} & 0 \\ 0 & G_{\parallel\Pi} \end{bmatrix}\zeta. \tag{B11}$$

APPENDIX C: THE SELECTION RULES FOR THE ORBITAL MOMENTUM

In the axially symmetric model of the electronic structure, there exist a set of selection rules, due to the dependence of

the wave function on the polar angle. We also imposed averaging with respect to the polar angle of light polarization, which provides a set of selection rules for the envelope orbital momenta of the states which take part in the transition,

$$\Delta(u)=\frac{1}{4}\begin{bmatrix} \delta_{l'_j,l_j-u}\delta_{l'_{j'},l_{j'}-u} & & & \\ \delta_{l'_j,l_j-u}\delta_{l'_{j'},l_{j'}+u} & \delta_{l'_j,l_j-u}\delta_{l'_{j'},l_{j'}-u} & & \\ -i\delta_{l'_j,l_j-u}\delta_{l'_{j'},l_{j'}-u} & -i\delta_{l'_j,l_j-u}\delta_{l'_{j'},l_{j'}+u} & \delta_{l'_j,l_j-u}\delta_{l'_{j'},l_{j'}-u} & \\ i\delta_{l'_j,l_j-u}\delta_{l'_{j'},l_{j'}+u} & i\delta_{l'_j,l_j-u}\delta_{l'_{j'},l_{j'}-u} & \delta_{l'_j,l_j-u}\delta_{l'_{j'},l_{j'}+u} & \delta_{l'_j,l_j-u}\delta_{l'_{j'},l_{j'}-u} \end{bmatrix}. \tag{C1}$$

Here, δ is the Kronecker symbol, u takes the values +1 and −1 in Eq. (16), and k labels the overlap matrix as shown in the leftmost column of Table VII.

The products of the component dipole matrix elements and the overlap matrix elements are selected by the rules arranged into the matrix,

$$\Lambda=\frac{1}{2}\begin{bmatrix} i\delta_{l'_j,l_j+1}\delta_{l'_{j'},l_{j'}} & -i\delta_{l'_j,l_j-1}\delta_{l'_{j'},l_{j'}} \\ i\delta_{l'_j,l_j-1}\delta_{l'_{j'},l_{j'}} & -i\delta_{l'_j,l_j+1}\delta_{l'_{j'},l_{j'}} \\ \delta_{l'_j,l_j+1}\delta_{l'_{j'},l_{j'}} & \delta_{l'_j,l_j-1}\delta_{l'_{j'},l_{j'}} \\ \delta_{l'_j,l_j-1}\delta_{l'_{j'},l_{j'}} & \delta_{l'_j,l_j+1}\delta_{l'_{j'},l_{j'}} \end{bmatrix}. \tag{C2}$$

*Electronic address: francois.peeters@ua.ac.be

[1] D. Bimberg and N. Ledentsov, J. Phys.: Condens. Matter **15**, R1063 (2003).
[2] P. Boucaud and S. Sauvage, C. R. Phys. **4**, 1133 (2003).
[3] A. D. Stiff, S. Krishna, P. Bhattacharya, and S. W. Kennerly, IEEE J. Quantum Electron. **37**, 1412 (2001).
[4] D. Krapf, S.-H. Kan, U. Banin, O. Millo, and A. Sa'ar, Phys. Rev. B **69**, 073301 (2004).
[5] S. Sauvage, P. Boucaud, F. Glotin, R. Prazeres, J.-M. Ortega, A. Lemaître, J.-M. Gérard, and V. Thierry-Mieg, Phys. Rev. B **59**, 9830 (1999).
[6] S. Sauvage, P. Boucaud, T. Brunhes, M. Broquier, C. Crépin, J.-M. Ortega, and J.-M. Gérard, Phys. Rev. B **66**, 153312 (2002).
[7] Y. C. Chang and R. B. James, Phys. Rev. B **39**, 12 672 (1989).
[8] F. Szmulowicz and G. J. Brown, Phys. Rev. B **51**, 13 203 (1995).
[9] M. Tadić and Z. Ikonić, Phys. Rev. B **52**, 8266 (1995).
[10] F. Szmulowicz, T. Oogarah, J. Ehret, K. Mahalingam, H. C. Liu, S. M. Hegde, J. Solomon, D. Tomich, G. Landis, and G. J. Brown, Phys. Rev. B **68**, 085305 (2003).
[11] T. Fromherz, W. Mac, C. Meisner, K. Brunner, G. Bauer, and G. Abstreiter, Physica E (Amsterdam) **13**, 2002 (2002).
[12] D. Bougeard, K. Brunner, and G. Abstreiter, Physica E (Amsterdam) **16**, 609 (2003).
[13] R. Bates, S. A. Lynch, D. J. Paul, Z. Ikonic, R. W. Kelsall, P. Harrison, S. L. Liew, D. J. Norris, A. G. Cullis, W. R. Tribe, and D. D. Arnone, Appl. Phys. Lett. **79**, 3639 (2001).
[14] T. Chakraborty and V. M. Apalkov, Adv. Phys. **52**, 455 (2003).
[15] S. Anders, L. Rebohle, F. F. Schrey, W. Schrenk, K. Unterrainer, and G. Strasser, Appl. Phys. Lett. **82**, 3862 (2003).
[16] N. Ulbrich, J. Bauer, G. Scarpa, R. Boy, D. Schuh, G. Abstreiter, S. Schmult, and W. Wegscheider, Appl. Phys. Lett. **83**, 1530 (2003).
[17] V. Tamosiunas, R. Zobl, J. Ulrich, K. Unterrainer, R. Colombelli, C. Gmachl, K. West, L. Pfeiffer, and F. Capasso, Appl. Phys. Lett. **83**, 3873 (2003).
[18] G. Scalari, S. Blaser, L. Ajili, J. Faist, H. Beere, E. Linfield, D. Ritchie, and G. Davies, Appl. Phys. Lett. **83**, 3453 (2003).
[19] J. Alton, S. Barbieri, J. Fowler, H. E. Beere, J. Muscat, E. H. Linfield, D. A. Ritchie, G. Davies, R. Köhler, and A. Tredicucci, Phys. Rev. B **68**, 081303(R) (2003).
[20] V. M. Apalkov and T. Chakraborty, Appl. Phys. Lett. **78**, 1973 (2001).
[21] S. Blaser, M. Rochat, M. Beck, D. Hofstetter, and J. Faist, Appl. Phys. Lett. **81**, 67 (2002).
[22] B. Kowalski, S. Nomura, C. Pryor, Y. Aoyagi, N. Carlsson, M.-E. Pistol, P. Omling, L. Samuelson, and W. Seifert, Phys. Rev. B **58**, 2026 (1998).
[23] Y.-Y. Lin and J. Singh, J. Appl. Phys. **92**, 6205 (2002).
[24] M. Tadić, F. M. Peeters, and K. L. Janssens, Phys. Rev. B **65**, 165333 (2002).
[25] M. Tadić, F. M. Peeters, K. L. Janssens, M. Korkusiński, and P. Hawrylak, J. Appl. Phys. **92**, 5819 (2002).
[26] C. Y. P. Chao and S. L. Chuang, Phys. Rev. B **46**, 4110 (1992).
[27] L. R. Ram-Mohan, K. H. Yoo, and R. L. Aggarwal, Phys. Rev. B **38**, 6151 (1988).
[28] U. Bockelmann and G. Bastard, Phys. Rev. B **45**, 1688 (1992).
[29] U. Bockelmann and G. Bastard, Phys. Rev. B **42**, 8947 (1990).
[30] T. Inoshita and H. Sakaki, Phys. Rev. B **56**, R4355 (1997).
[31] S. Hameau, Y. Guldner, O. Verzelen, R. Ferreira, G. Bastard, J. Zeman, A. Lemaître, and J. M. Gérard, Phys. Rev. Lett. **83**, 4152 (1999).

[32] E. A. Zibik, L. R. Wilson, R. P. Green, J.-P. R. Wells, P. J. Phillips, D. A. Carder, J. W. Cockburn, M. S. Skolnick, M. J. Steer, H. Y. Liu, and M. Hopkinson, Physica E (Amsterdam) **21**, 405 (2004).

[33] P. Bhattacharya, S. Krishna, J. Phillips, P. J. McCann, and K. Namjou, J. Cryst. Growth **227**, 27 (2001).

[34] I. Vurgaftman, J. R. Meyer, and L. R. Ram-Mohan, J. Appl. Phys. **89**, 5815 (2001).

[35] *Semiconductors: Group IV Elements and III-V Compounds*, edited by O. Madelung (Springer, Berlin, 1991).

[36] W. Ekardt, K. Lösch, and D. Bimberg, Phys. Rev. B **20**, 3303 (1979).

[37] P. Lawaetz, Phys. Rev. B **4**, 3460 (1971).

[38] H. C. Liu, C. Y. Song, A. J. SpringThorpe, and J. C. Cao, Appl. Phys. Lett. **84**, 4068 (2004).